Chemical Science

ROYAL SOCIETY OF CHEMISTRY

EDGE ARTICLE

View Article Online
View Journal | View Issue

Cite this: *Chem. Sci.*, 2025, **16**, 18642

All publication charges for this article have been paid for by the Royal Society of Chemistry

Received 16th August 2025
Accepted 5th September 2025

DOI: 10.1039/d5sc06255a

rsc.li/chemical-science

An atomically precise $Au_{10}(DPPF)_4PPh_3$ cluster catalyst for N-hydroformylation of amines

Guangjun Li,†[ab] Guoao Li,†[a] Xinyi Liang,[a] Yiqi Tian,[a] Jinzhi Lu,[a] Xinyi Xu,[a] Xu Liu,[a] Jing Ma,[a] Shuhua Li *[a] and Yan Zhu *[ac]

Heterogeneous catalysis is crucially important for the well-being of society, and new catalysts are continuously discovered to improve chemical processes. Here we report a catalytic system based on an atomically precise $Au_{10}(DPPF)_4PPh_3$ (DPPF = bidentate 1,1′-bis(diphenylphosphino)ferrocene) cluster, where two functional units are combined into one catalyst for N-hydroformylation of pyrrolidine with CO_2 and H_2. The two units execute their respective roles, including two types of ligands that mediate the structural framework and further reinforce the catalytic stability of the cluster, and a metal core consisting of ten gold atoms that are all potentially active sites participating in the hydrogenation of CO_2 toward the key intermediate, such as formic acid. Sequentially, formylation proceeds *via* a relay migration of protons along a proposed transition state originating from the intermediate and pyrrolidine, thereby breaking the N–H bond and constructing the C–N bond. The synergy between the active sites and the neighbouring environment therefore enables optimal activity and stability of the cluster catalyst, outperforming most catalysts reported under comparable conditions.

Introduction

Catalysis is immensely important for chemical transformations, and approximately 90% of chemicals are synthesized involving at least one catalytic process. It is therefore not surprising that new catalysts are continually required to improve catalytic performances with respect to activity, selectivity, stability and more. Metal nanoparticles are the most important catalysts for the majority of current chemical processes, such as partial oxidation,[1,2] selective hydrogenation,[3,4] electrocatalysis,[5,6] fuel generation,[7] *etc.* Additionally, single-atom catalysts are attracting growing attention due to their 100% atom efficiency.[8–10] Between the nanoparticles and singe-atom catalysts, there are atomically precise metal clusters with crystallographically solved structures, which have constituted a new generation of metal catalysts and provided tremendous opportunities in catalysis science.[11–17] Such clusters not only permit a precise correlation of their structures with catalytic properties but also allow for identification of catalytically active sites. More importantly, they exhibit intermediate properties between molecular behavior and metallic properties, thereby integrating catalysis of homogeneous organometallic-based complexes and heterogeneous metal nanoparticles.

Formamides are widely used as solvents and intermediates for value-added chemicals such as pharmaceuticals, fungicides, N-heterocycles and isocyanates.[18–20] Due to the cost, toxicity-free, abundance and widespread accessibility, the N-hydroformylation of amines coupled with CO_2 hydrogenation as a renewable carbonyl feedstock has attracted much attention. Since the initial report by Adkins *et al.* on nickel-catalyzed synthesis of formamides with CO_2 and H_2,[21] a series of transition-metal catalysts such as ruthenium, iridium, palladium and copper have been developed.[22–41] For example, Noyori *et al.* in 1994 reported a $RuCl_2[P(CH_3)_3]_4$ homogeneous catalyst and a turnover number (TON) of 370 000 for *N*,*N*-dimethylformamide (DMF) synthesis was obtained in supercritical CO_2 with 8 MPa H_2.[22] Ding and coworkers developed a Ru–pincer complex homogeneous catalyst with a TON of 1 940 000 for DMF synthesis (120 °C, $P_{CO_2} = P_{H_2} = 3.5$ MPa).[23] Due to the difficulties of the separation and recyclability of organometallic-based complexes, heterogeneous catalysts were explored. Ma *et al.* reported an isolated Ir catalyst supported on a nanodiamond/graphene hybrid, achieving a TON of 6 340 000 for methylmorpholine at 150 °C and 4.8 MPa ($CO_2 : H_2 = 1 : 1$).[27] Shi and coworkers successfully constructed Cu_2O/Cu interface sites, which showed high yields for diverse amine substrates at 150 °C and 4 MPa ($CO_2 : H_2 = 1 : 3$).[34,35] However, heterogeneous catalysts usually suffer from the requirement of additives and harsh

[a]*Key Laboratory of Mesoscopic Chemistry of Ministry of Education, State Key Laboratory of Coordination Chemistry, School of Chemistry and Chemical Engineering, Nanjing University, Nanjing 210093, China. E-mail: zhuyan@nju.edu.cn; shuhua@nju.edu.cn*

[b]*State Key Laboratory of Chemistry and Utilization of Carbon Based Energy Resources, College of Chemistry, Xinjiang University, Urumqi 830017, China*

[c]*State Key Laboratory of Low Carbon Catalysis and Carbon Dioxide Utilization, Lanzhou Institute of Chemical Physics, Chinese Academy of Sciences, Lanzhou, 730000, China*

† These authors contributed equally to this work.

conditions.[36–41] Therefore, integrating the advantages of homogeneous and heterogeneous catalysis into a catalytic system with high activity and excellent recyclability are highly desirable.

In this work, we synthesize an atomically precise metal cluster, determine its chemical formula, and solve its total structure. This novel cluster is unique in the library of metal clusters and has "open" metal sites, and thereby all metal atoms of the cluster are potentially active centers. Notably, this cluster exhibits exquisite specificity for molecular recognition, providing an opportunity for oriented catalysis toward the customized product. Exemplified by the N-hydroformylation of pyrrolidine with CO_2 and H_2, the cluster catalyst not only exhibits highly catalytic efficiency, comparable to homogeneous single-metal complexes, but also is conveniently recycled and reused, holding promise for industrial applications in heterogeneous catalysis.

Results and discussion

The $Au_{10}(DPPF)_4PPh_3$ (hereinafter Au_{10}) cluster, protected by bidentate 1,1′-bis(diphenylphosphino)ferrocene (abbreviated as DPPF) and triphenylphosphine (PPh_3), was synthesized for the first time, and its total structure was determined by single-crystal X-ray crystallography. As shown in Fig. 1a and Table S1, the cluster belonged to the $P2_1/c$ space group and consisted of ten gold atoms, four DPPF ligands and one PPh_3 ligand. Ten gold atoms made up the metal core of the cluster, where only one Au atom was situated in the center and established metallic bonds with the Au atoms around it, and another nine Au atoms were bonded to phosphines to create surface-coordinated units. Specifically, as shown in Fig. 1b, for bidentate DPPF ligands, one ligand was bonded to the top and waist Au atoms (Au1 and Au2), one was coordinated with the bottom two Au atoms (Au5 and Au6), and the remaining two DPPF ligands were combined with the waist and bottom Au atoms (Au3 and Au4, Au7 and Au8). The PPh_3 ligand was coupled with the last waisted Au atom (Au9). In addition, one Cl^- served as the counterion in the cluster.

Electrospray ionization mass spectrometry (ESI-MS) further confirmed the composition and molecular formula of the cluster (Fig. 1c). The major peak located at 2225m/z corresponded to $[Au_{10}(DPPF)_4PPh_3\text{-}e]^{2+}$, which was well compatible with the formula of the single crystal. Moreover, the isotopic experimental spectrum of the Au_{10} cluster ion peak matched the computational simulation spectrum exactly (the inset in

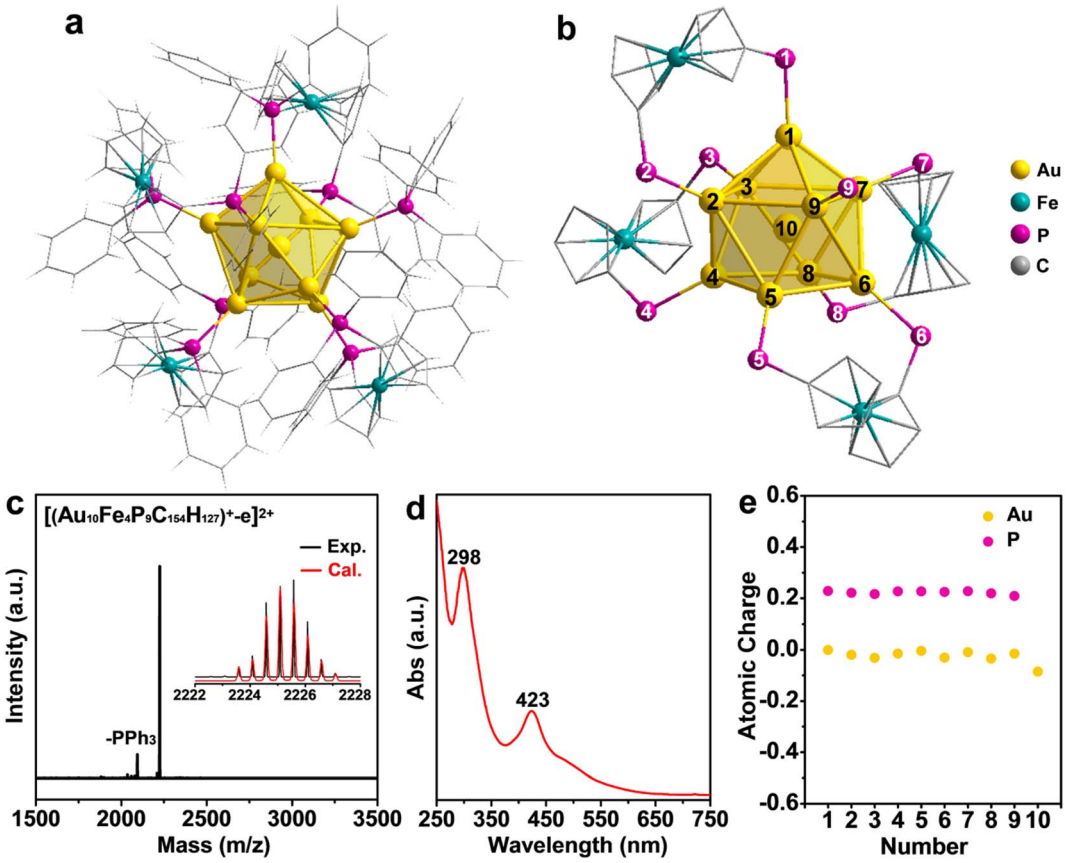

Fig. 1 (a) Total structure of the $Au_{10}(DPPF)_4PPh_3$ cluster. (b) The coordinated modes of DPPF and PPh_3 ligands attached to Au atoms. Benzene rings and hydrogen atoms are omitted for clarity. (c) ESI-MS profiles of the cluster. The illustration compares experimental (black) and theoretical simulation (red) isotopic patterns of the cluster. (d) UV-vis absorption spectrum of the $Au_{10}(DPPF)_4PPh_3$ cluster. (e) The Hirshfeld charge distribution of each Au atom and its adjacent P atom labelled in (b).

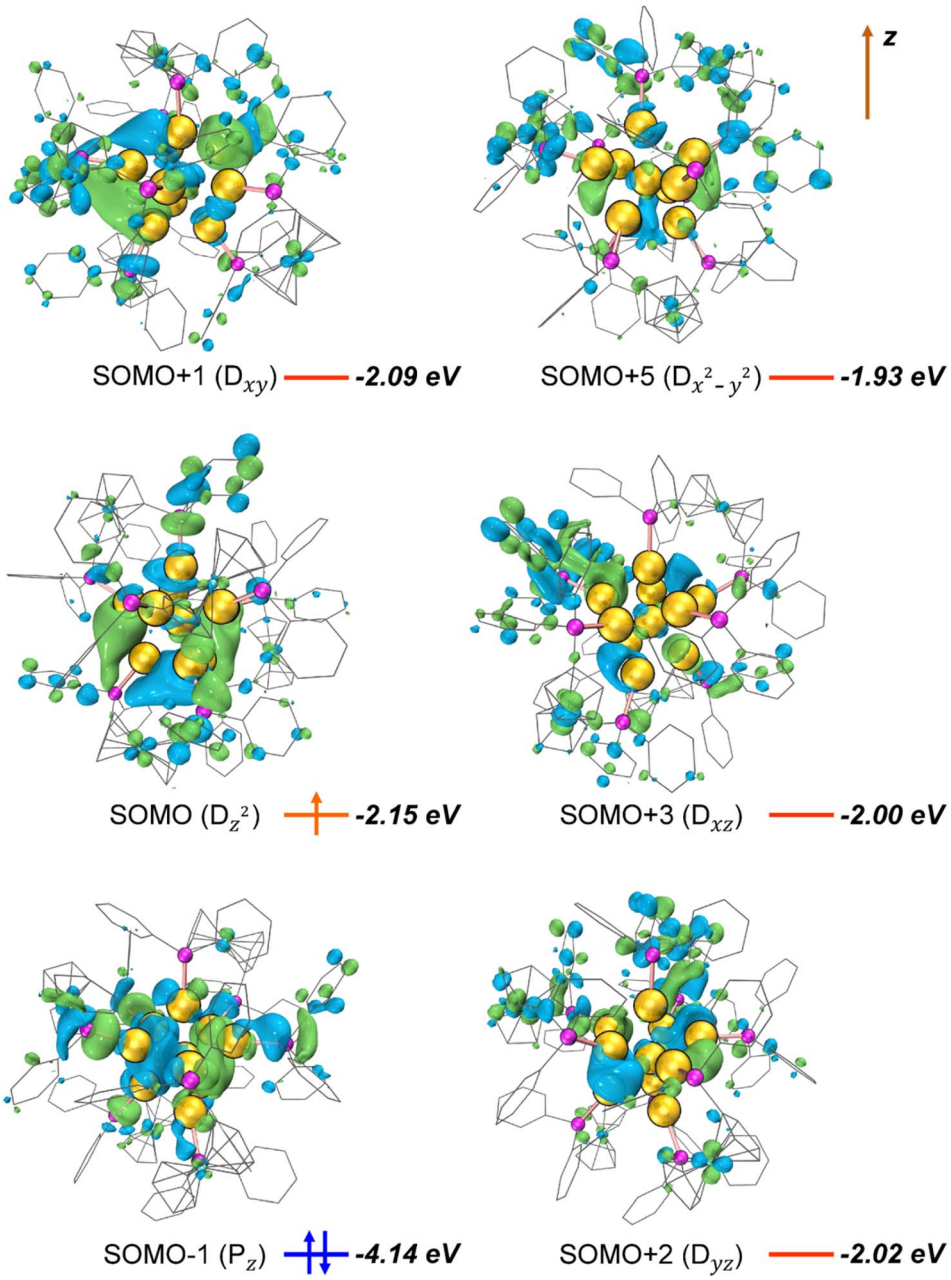

Fig. 2 Calculated frontier Kohn–Sham orbitals of $Au_{10}(DPPF)_4PPh_3$ with an isosurface value of 0.02 a.u. at the SMD(MeCN)-RI-ROTPSS/def2-SVP level.

Fig. 1c). Notably, the additional small peak at 2094m/z was assigned to the production of $[Au_{10}(DPPF)_4\text{-}e]^{2+}$ due to the removal of the PPh_3 ligand when the MS measurement was processed. As can be seen from the TG profile (Fig. S1), $Au_{10}(DPPF)_4PPh_3$ exhibited substantial thermal stability below 150 °C, indicating its structural integrity. Thermal decomposition initiated above this threshold, with sequential PPh_3 ligand dissociation, followed by DPPF ligand release above 275 °C. Near-complete deligation occurred above 485 °C, resulting in a cumulative mass loss of 54.8%. The Au_{10} cluster exhibited a distinctive UV-vis spectrum with two obvious absorption peaks at 423 and 298 nm and a weak acromion at ~500 nm (Fig. 1d). Based on the optimized geometries of the Au_{10} cluster shown in Fig. S2 at the PBE0-D3/6-31G(d) level (LanL2DZ for Au and Fe), the distribution of Hirshfeld charge for Au_{10} was calculated (Fig. 1e and Table S2), which showed that the Au sites of Au_{10} were weakly negatively charged and the charges of surface Au sites were essentially equal. We recognized that the ten Au atoms of the cluster might be all potentially active sites participating in a chemical process.

To examine the molecular orbital characteristics of the Au_{10} cluster in more depth, the frontier Kohn–Sham orbitals were calculated under the restricted open-shell self-consistent field scheme. The singly occupied molecular orbital (SOMO) and its

neighboring orbitals are visualized in Fig. 2. The SOMO and the other four virtual orbitals (SOMO+1, SOMO+2, SOMO+3 and SOMO+5), with similar orbital energies, exhibited superatom features of a complete group of d-orbitals to some extent, while the doubly occupied SOMO−1 orbital somehow showed superatom features of a p_z-orbital.[42,43]

We next began our investigation into catalysis of the Au_{10} cluster as a new catalyst for N-hydroformylation of amines with CO_2 hydrogenation. As displayed in Fig. 3a, exemplified by the pyrrolidine hydroformylation, the Au_{10} cluster was indeed robust and gave rise to a high yield of formylpyrrolidine at 100 °C and 6 MPa ($CO_2 : H_2 = 1 : 3$). Notably, the DPPF ligand had no activity, revealing that the Fe atoms of DPPF were not active sites. The reference catalyst such as the gold precursor ($AuPPh_3Cl$) showed an extremely low activity and totally degraded during the reaction (Fig. S3). Although another gold precursor ($HAuCl_4 \cdot 4H_2O$) exhibited a slight activity, the majority degraded and turned into black precipitate following the reaction. The catalytic performance of gold nanoparticles (Au NPs) was also assessed, as shown in Fig. 3a, which showed much lower activity compared to the Au_{10} cluster. In addition, as shown in Fig. S4a, when dichloroethane (DCE) and dimethyl sulfoxide (DMSO) were used as solvents, Au_{10} clusters showed little formylation activity. In contrast, the activity of Au_{10} clusters was essentially enhanced in ethanol (EtOH) and acetonitrile (MeCN) solvents. It can be seen from Fig. S4b that the UV-vis absorption peaks of Au_{10} clusters totally vanished in DMSO and DCE, indicating the cluster fluctuation and instability in the two cases, while UV-vis spectra of the clusters in the EtOH and MeCN systems showed no change, suggesting that the clusters were stable in the latter two cases. Obviously, just as the cluster structure was retained under reaction conditions, the Au_{10} cluster can show its unique high activity for N-hydroformylation.

Moreover, the activity of Au_{10} clusters followed a typical volcanic curve, as shown in Fig. S5, showing notable activity solely upon reaching 80 °C, with activity basically peaking at 100 °C, then declining at 120 °C, and finally falling below 50% at 150 °C. Additionally, the formylation selectivity of the catalyst gradually diminished, while the methylation products

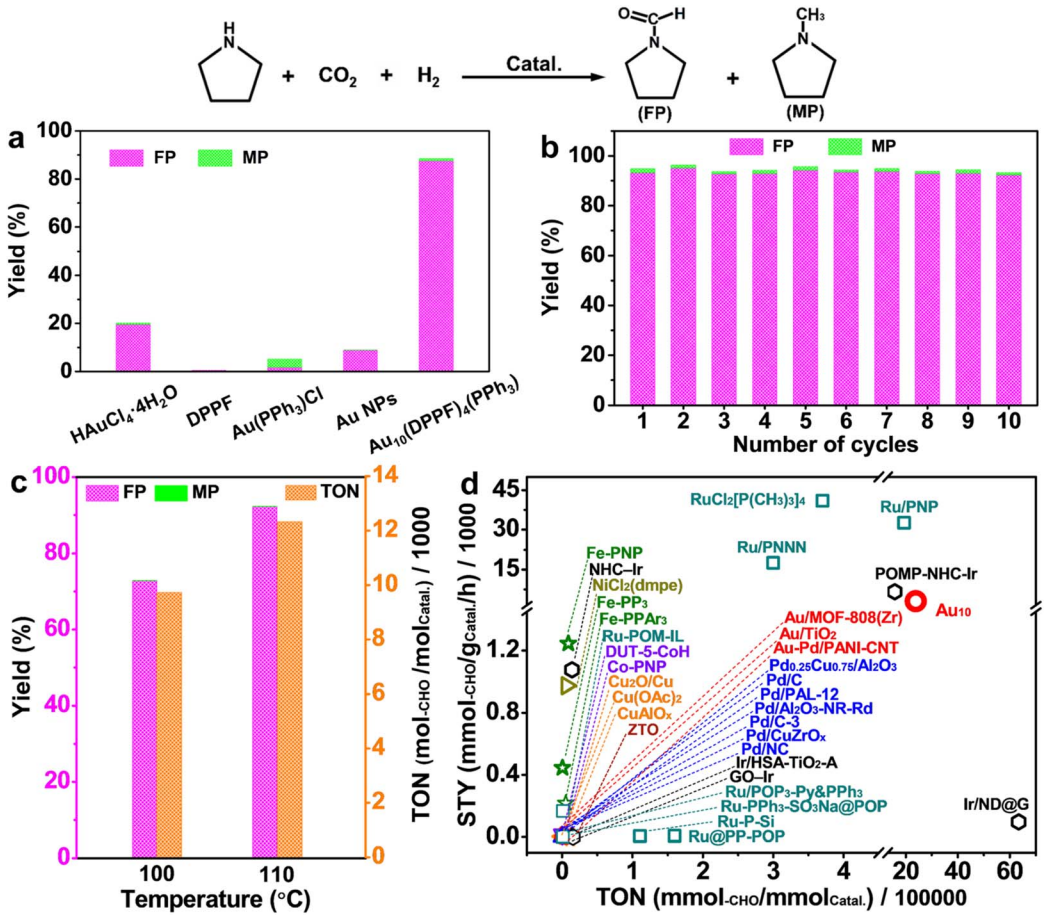

Fig. 3 (a) Catalytic activity of $Au_{10}(DPPF)_4PPh_3$, gold precursors, Au NPs and DPPF ligands for the pyrrolidine hydroformylation with CO_2 and H_2. Reaction conditions: 2 mmol pyrrolidine, 0.1 mol% Au or 0.4 mol% DPPF, 5 mL acetonitrile, 6 MPa ($CO_2 : H_2 = 1 : 3$), 100 °C, 24 h. (b) Recyclability of Au_{10} clusters. Reaction conditions: 2 mmol pyrrolidine, 0.1 mol% Au, 5 mL acetonitrile, 8 MPa, 100 °C, 15 h. (c) Catalytic performances of Au_{10} clusters for pyrrolidine hydroformylation with CO_2 and H_2 in the solvent-free system. Reaction conditions: 30 mmol pyrrolidine, 10 mg cluster, 8 MPa, 15 h. (d) Comparison of catalytic performances of different catalytic systems reported for N-hydroformylation of amines with CO_2 and H_2. Note: STY: space-time yield; –CHO: formylation products. The reaction parameters of these catalytic systems are summarized in Table S3.

Table 1 The optimization of catalytic performances of Au_{10} clusters for pyrrolidine hydroformylation with 8 MPa CO_2 and H_2 ($CO_2 : H_2 = 1 : 3$) in the solvent-free reaction systems

Entry	Pyrrolidine (mmol)	Catalyst weight (mol%/mg)	Temperature (°C)	Time (h)	Yield (%)	TON (mol_{CHO} per $mol_{catal.}$)	TON (mol_{CHO} per $g_{catal.}$)	TOF (mol_{CHO} per $mol_{catal.}$ per h)	TOF ($mmol_{CHO}$ per $g_{catal.}$ per h)
1	30	0.007/10	100	15	72.9	9733	2.19	649	146
2	30	0.007/10	110	15	92.3	12 323	2.77	821	185
3	30	0.0007/1	110	15	52.5	70 093	15.7	4673	1050
4	300	0.00007/1	110	88	45.3	604 806	135.9	6873	1544
5	300	0.00007/1	110	176	85.6	1 142 857	255.9	6493	1454
6	550	0.00002/0.5	110	176	48.2	2 359 590	530.2	13 407	3012

increased as the reaction temperature rose above 100 °C, suggesting that the increase in temperature was conducive to deep hydrogenation of formylation products. It further implied that the activity of the Au_{10} catalyst highly depended on the structural sturdiness. The catalytic activity of Au_{10} clusters was also influenced by the reaction pressure (Fig. S6). It is noteworthy that the Au_{10} catalyst can be easily recovered by the addition of a small quantity of water and straightforward centrifugation after the solvent is extracted by vacuum distillation. In Fig. 3b and S7, the formylation product yield of the Au_{10} catalyst remained essentially unchanged for a duration of up to 10 cycles, indicating the excellent recyclability of Au_{10} clusters that can be comparable to heterogeneous catalysts. Time-resolved UV-vis spectra and *in situ* Fourier-transformed infrared (FTIR) spectra of the Au_{10} clusters at reaction temperatures were recorded to probe the changes of the structure and ligands of the clusters (Fig. S8), which illustrated that the Au_{10} clusters were intact and no ligands were detached from the clusters under reaction conditions. The observations suggested the intimate coordination between the surface ligands and the metal core, thereby strengthening active sites of the cluster against its deactivation during the reactions.

More notably, unlike the traditional organic solvent-mediated catalytic reaction system, the Au_{10} clusters showed excellent catalytic properties in the solvent-free system (Fig. 3c), which indicated the potential scalability of Au_{10} clusters in practical applications. The maximum formylation yield with a TON value over 12 000 can be observed at a reaction temperature of 110 °C, where Au_{10} was still robust (Fig. S9a). Impressively, although prolonged reaction time was needed, further decreasing the cluster loading could significantly improve TON values, and a very high TON value of up to 2 359 590 can be achieved under the optimal conditions (Table 1). UV-vis spectra confirmed structural integrity of spent Au_{10} clusters, as evidenced by retention of characteristic absorption bands across varying substrate concentrations (Fig S9b). Manifestly, the catalytic capability of Au_{10} clusters was indeed superior to that of metal-based (Ru, Ir, Au, Pd, Cu, Fe, Co, *etc.*) catalysts reported under comparable conditions (Fig. 3d and Table S3).

With the precise structure of the cluster in hand, we initiated mechanistic studies to unveil fundamental insights into the Au_{10} cluster that can integrate homogeneous and heterogeneous catalysis. X-ray photoelectron spectroscopy (XPS) was first utilized to measure the charge states of Au and Fe elements of the Au_{10} cluster. As depicted in Fig. S10a, the binding energy of Au 4f on the Au_{10} cluster was higher than that of metallic gold (84.0 eV), indicating positively charged gold in the cluster, *i.e.*, $Au^{\delta+}$ ($0 < \delta < 1$).[44,45] Furthermore, little discernible discrepancy of the Au $4f_{7/2}$ binding energy on the Au_{10} cluster after the catalytic reaction suggested that the electronic configuration of the cluster remained relatively stable during the reaction. The binding energy of Fe $2p_{3/2}$ on the DPPF ligand was 708.0 eV (Fig. S10b), which was consistent with the literature report.[46] Besides, no shift of binding energy of Fe 2p on the spent sample further corroborated the robustness of the cluster under reaction conditions.

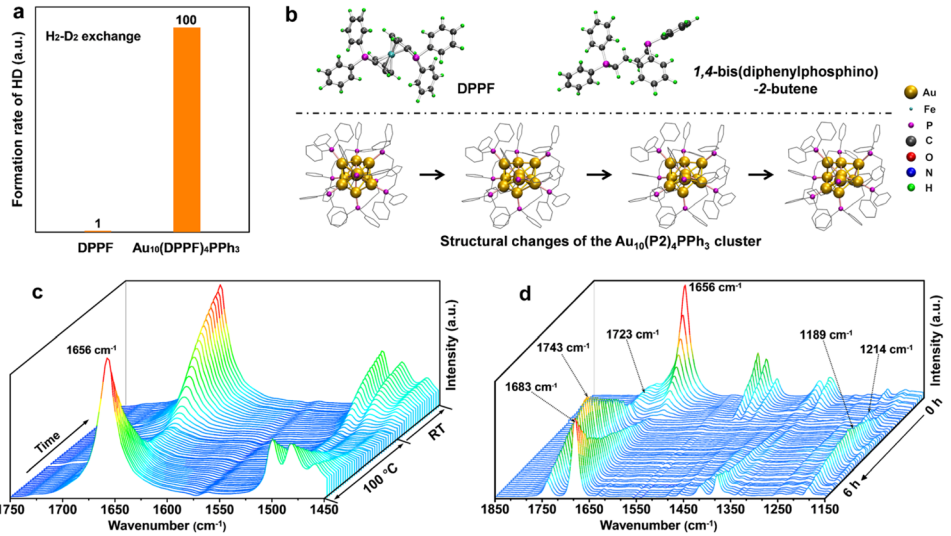

Fig. 4 (a) The normalized HD formation rate during the H_2–D_2 exchange reaction for the $Au_{10}(DPPF)_4PPh_3$ cluster and the DPPF ligand, respectively. (b) Ligand substitution calculations of the Au_{10} cluster. The upper panel shows the structures of the DPPF ligand (left) and the simplified P2 ligand (right). The lower panel shows the structural changes of the $Au_{10}(P2)_4PPh_3$ cluster during optimizations (from left to right). (c) Time-resolved *in situ* FTIR spectra obtained from the reaction of pyrrolidine and CO_2 performed in the high-pressure liquid cell system without the catalyst. (d) Time-resolved *in situ* FTIR spectra corresponding to reaction intermediate species formed in the high-pressure liquid cell during the pyrrolidine hydroformylation reaction with CO_2 and H_2 catalysed by Au_{10} clusters.

The adsorption and activation behavior of H_2 on the Au_{10} cluster was explored using H_2–D_2 exchange experiments. As shown in Fig. 4a, the formation rate of HD on the Au_{10} cluster was much higher than that on the DPPF ligand, suggesting that the hydrogen could be significantly adsorbed and activated onto the Au sites of the Au_{10} cluster.[47] Notably, the H_2–D_2 exchange signals were hardly observed over the DPPF ligand, indicating that the DPPF ligand could not activate H_2, which was essentially in agreement with the catalytic result of the pure DPPF ligand as a catalyst (Fig. 3a). To further reveal the role of the DPPF ligand, we substituted the ferrocene group in Au_{10} with the *trans*-2-butaene group that kept the geometric properties of ferrocene, the corresponding model ligand was named P2 (Fig. 4b). The substituted P2 ligands was first pre-optimized and then optimized the $Au_{10}(P2)_4PPh_3$ cluster. The average P–P distance of the P2 ligands varied little from 5.38 Å to 5.27 Å, while the Au_{10} structure changed significantly, with the RMSD of the 10 Au atoms reaching 0.611 Å. Besides, the average Hirshfeld charges of the 10 Au atoms changed from −0.047 to −0.037 after the ligand substitution, indicating that the ferrocene group shared more electrons with the Au atoms than ordinary phosphine ligands. These results indicated that although the DPPF ligands did not directly participate in the reaction mechanism, they made significant contributions to the structural stability of the Au_{10} cluster. The 10 Au atoms could not form the compact cluster core without DPPF. The coordination mode of CO_2 onto the Au_{10} clusters was also detected by *in situ* FTIR spectroscopy (Fig. S11). When CO_2 was introduced into the IR cell with the Au_{10} clusters, the IR spectra did not obviously change, indicating that the Au_{10} cluster could not directly activate CO_2 molecules.

To further probe the reactant intermediates and the evolution process of pyrrolidine hydroformylation with CO_2 and H_2 over the Au_{10} clusters, *in situ* FTIR studies were conducted using a temperature-controlled system with a high-pressure liquid cell. As shown in Fig. 4d, the representative bands at 1656 cm^{-1} assigned to ammonium carbamate[48,49] appeared as soon as the reaction began, and then rapidly vanished with reaction time. Supported by the time-independent *in situ* FTIR spectra from the reaction of CO_2 and pyrrolidine without the catalyst (Fig. 4c), pyrrolidine existed as ammonium carbamate at room temperature by capturing CO_2, and was released at reaction temperatures (100 or 110 °C). At the initial stage of reaction, as the band at 1656 cm^{-1} disappeared, a new band located at ~1723 cm^{-1}, together with another new band at 1214 cm^{-1}, emerged simultaneously and their intensities enhanced gradually with reaction time. By calibrating through standard substances under identical catalytic conditions, the bands at ~1723 and 1214 cm^{-1} were respectively assigned to the stretching vibrations of carbonyl and carbon–oxygen bonds from formic acid (Fig. S12a). The results indicated that formic acid was initially the key intermediate. In succession, the band at ~1723 cm^{-1} substantially shifted to 1743 cm^{-1} accompanied by the rapid enhancement of intensity, whereas the intensity of the band at 1214 cm^{-1} decreased with time, implying that formic acid could convert into more stable intermediate species as the reaction proceeded. Meanwhile, a new band emerging at 1189 cm^{-1} showed the same trend of intensity as the new strong band at 1743 cm^{-1}. Both of them could be respectively assigned to the typical absorption of the carbon–oxygen bond and the carbonyl group,[50] suggesting that the stable intermediate species likely contained the ester group. To further identify the stable intermediate species, when the intensities of bands at

1743 and 1189 cm^{-1} reached their maxima, heating was stopped, and the IR spectra were collected during the cooling process. As illustrated in Fig. S13a, the intensities of the bands assigned to the stable intermediate species slightly modulated with cooling. Meanwhile, the characteristic band belonged to ammonium carbamate at ~1656 cm^{-1} faintly returned with cooling, indicating that tiny residual pyrrolidine reacted with CO_2. Thus, we speculated that most pyrrolidine was involved in the generation of stable intermediate species and hence the intermediate contained the amino group. From the above results, it was therefore deduced that the stable intermediate associated with both the ester and amino groups likely derived from the interaction between formic acid and pyrrolidine, which could be further verified by our calculation studies. When the IR bands reached their maxima, the signals of the double bonds assigned to the stable intermediate subsequently began to decrease gradually (Fig. 4d), while the signals of the formylated product characterized by the carbonyl band at 1683 cm^{-1} (Fig. S12b) constantly increased, indicating the conversion of the stable intermediate species toward the products. It was noteworthy that two additional small bands were probed at 1622 and 1636 cm^{-1}, and their intensities subtly increased with the conversion of the stable intermediate species (Fig. S13b). The former at 1622 cm^{-1} was confirmed to be the signal of by-product H_2O by the calibration (Fig. S12c), and the latter at 1636 cm^{-1} was speculated to be the carbonyl group that was assigned to another intermediate species that was generated during the conversion of the stable intermediate to the products. Taken overall, the IR data unveiled that in terms of the Au_{10} catalyst system, formic acid was first generated and then interacted with pyrrolidine to form the stable intermediate species that were further transformed toward the formylated product.

Based on the precise structure of the $Au_{10}(DPPF)_4PPh_3$ cluster, the activation modes of reactants and the reaction intermediates obtained, density functional theory (DFT) and semi-empirical quantum chemistry calculations were utilized to further shed light in detail on the molecular-level reaction mechanism of pyrrolidine hydroformylation with CO_2 and H_2 on the Au_{10} cluster. First, to describe the equilibrium structures of Au_{10}-containing species, the geometry of the Au_{10} cluster was optimized at the semi-empirical GFN1-xTB level, where the 10 Au atoms showed small differences from the X-ray crystal structure (RMSD = 0.046 Å) and from DFT optimized structure

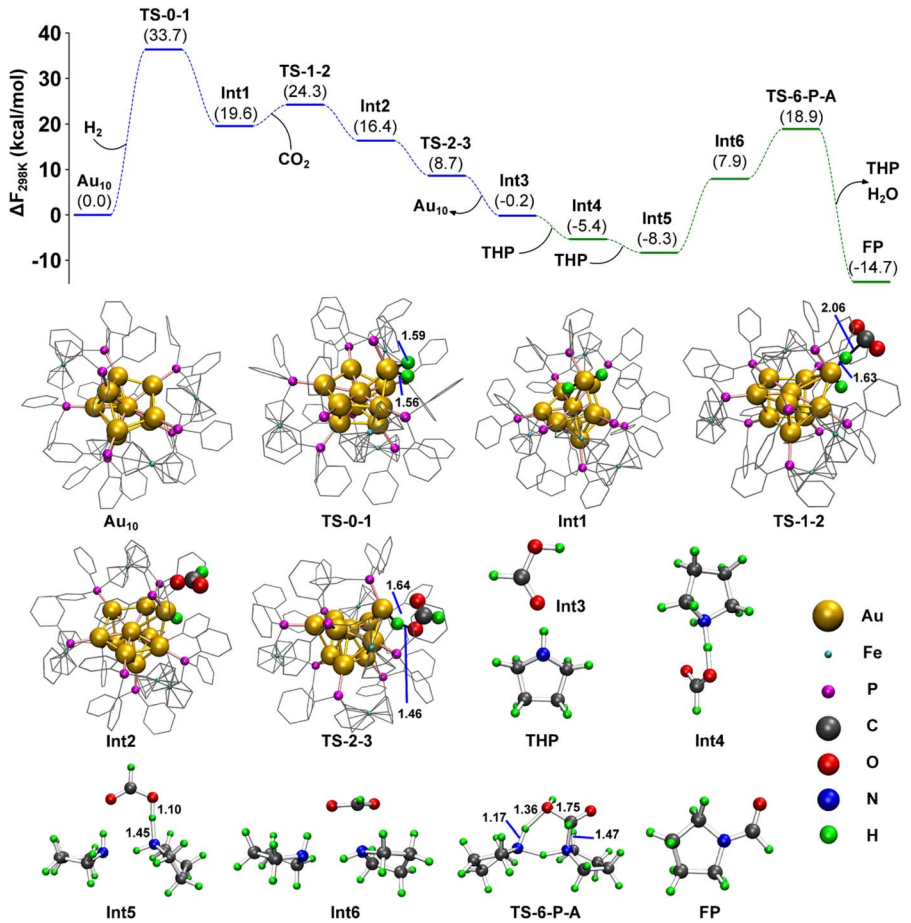

Fig. 5 The upper panel shows the Helmholtz free energy profile and the lower panel shows the corresponding molecular structures of intermediates and transition states from the pyrrolidine hydroformylation with CO_2 and H_2 on the Au_{10} cluster catalysts. Atomic distances are labeled in Å. Note: THP: pyrrolidine, FP: formylpyrrolidine. The computational level is SMD(MeCN)-RI-TPSS-D4/def2-SVP//ALPB (MeCN)-GFN1-xTB for the blue part of the profile and SMD(MeCN)-PBE0-D3/6-311 +G(d,p)//PBE0-D3/6-31G(d) for the green part.

(RMSD = 0.225 Å) at the PBE0-D3/6-31G(d) (LanL2DZ) level (Fig. S14). Then we located the preliminary reaction pathways at the GFN1-xTB level with the combined molecular dynamics and coordinate driving method (MD/CD)[51,52] implemented in the Automated Design of Chemical Reactions (ADCR) program, and further DFT calculations were performed to yield more accurate single-point electronic energies. The Helmholtz free energy profile of the main pathway of pyrrolidine hydroformylation with CO_2 and H_2 catalyzed by the Au_{10} cluster is illustrated in Fig. 5 and Table S4. The first step was the activation of H_2 at the PPh_3-coordinated surface Au atom *via* TS-0-1 to afford the Au–H intermediate Int1, with an activation barrier of 33.7 kcal mol^{-1}. The direct dissociation of the ligand PPh_3 from the Au_{10} cluster was energetically unfavorable, with a heat uptake of 31.2 kcal mol^{-1} on the Helmholtz free energy and a subsequent H_2 activation barrier of up to 60.0 kcal mol^{-1} (Table S4). Then, the reduction of CO_2 can easily occur through the cascade hydride transfer (TS-1-2) and proton transfer (TS-2-3) to form the formic acid Int3 (HCOOH) and to restore the Au_{10} cluster. The relative activation barrier is only 4.7 kcal mol^{-1} with respect to Int1 and CO_2. The overall procedure to form HCOOH was exothermic by 0.2 kcal mol^{-1}. Along this pathway, the DPPF-coordinated surface Au atoms and the central Au atom of the cluster might also participate in the HCOOH formation, which involved slightly higher activation barriers (TS-0-1b and TS-0-1c in Fig. S15).

The HCOOH intermediate could be further captured by pyrrolidine (THP) molecules to form the Brønsted acid–base aggregates Int4, Int5 and Int6, with the calculated Hirshfeld charges on the carbon atom of the formic acid as 0.174, 0.159 and 0.175, respectively. They were stable intermediate species indicated by FTIR results, which could undergo the amidation process to yield the final formylated product (FP) directly or with assistance from small molecules inside the reaction system. It was also found that HCOOH and pyrrolidine could convert directly into formylated products at 100 °C without Au_{10} clusters, which was consistent with the experimental results (Fig. S16). Three amidation modes were proposed in Fig. S17: (a) one THP molecule assisted amidation *via* a six-membered-ring transition state TS-6-P-A (intrinsic reaction coordinate (IRC) curve shown in Fig. S18), (b) one H_2O molecule assisted amidation *via* a six-membered-ring transition state TS-6-P-B, and (c) direct amidation *via* a four-membered-ring transition state TS-6-P-C. The corresponding Helmholtz free energy barriers were 27.2, 33.0 and 40.0 kcal mol^{-1}, respectively. The amidation of the main intermediate Int5 was exothermic by 6.4 kcal mol^{-1} (Fig. 5). Thus, we speculate that molecules containing OH or NH groups (*i.e.*, H_2O or THP) could promote the formation of a six-membered proton transfer transition state between the substrate and HCOOH, thereby accelerating the breaking of the N–H bond and the formation of the C–N bond. In addition, the lower energy barrier of the transition state TS-6-P-A accounted for the experimental fact that the high yield of the formylated product can be obtained over the Au_{10} catalyst in the absence of solvent (Fig. 3c).

Interestingly, the Au_{10} cluster exhibited exquisite recognition for amine molecules, thereby achieving specificity for the customized products. As shown in Fig. S19a, the Au_{10} cluster catalyst showed the highest activity for the pyrrolidine hydroformylation, while the activity almost vanished when the *ortho* position of pyrrolidine was substituted by carbonyl. The conversion of piperidine was also significantly diminished by swapping out the *para*-C of piperidine for an oxygen atom (morpholine). Relative to non-substituted heterocyclic aliphatic amines, the straight chain amines (*e.g.*, Et_2NH and Me_2NH) tended to react less with CO_2 and H_2 over the cluster catalysts, and *N*-methylaniline had little conversion. The reaction efficiency of secondary amine hydroformylation with CO_2 and H_2 on the Au_{10} catalyst was shown in a descending sequence: pyrrolidine > piperidine > Me_2NH > morpholine > Et_2NH > *N*-methylaniline ~ pyrrolidone. Fig. S19 showed that the Helmholtz free energy barriers of pyrrolidone and *N*-methylaniline with little yield of amidation were as high as 58.1 and 35.6 kcal mol^{-1}, respectively, and the overall amidation processes were only exothermic by 2.4 and 5.3 kcal mol^{-1}. The strong hydrophilicity of morpholine ($\log P = -0.86$) was also responsible for the low yield of its amidation, despite a low energy barrier of formylation (25.2 kcal mol^{-1}). Besides, the reaction energy barrier might be related to the alkalinity of the N atom on the substrate. According to the transition state of proton transfer (Fig. S19b), it can be inferred that the stronger the alkalinity of the N atom on the substrate, the lower the energy barrier of the transition state. Thus, it was speculated that the reaction thermodynamics, the energy barrier and the $\log P$ value of the substrate molecules might together affect the amidation processes.

Conclusions

In summary, we report the catalytic coupling of the DPPF ligand anchored Au_{10} cluster catalyst, in which the surface ligands manipulate the charge distribution between the metal core and the ligand and further support the cluster framework against structural collapse and sintering during catalytic processes, and thereby the Au_{10} core can give its excellent performance for the hydrogenation of CO_2 toward the crucial intermediate. The surrounding environment that has access to the active sites of the cluster sequentially plays a positive par in facilitating the formylation process of the intermediates and amine. The combined catalysis from the cooperative communication within the cluster catalyst and the interplay between the active center and the neighbouring environment ultimately brings the $Au_{10}(DPPF)_4PPh_3$ cluster to a highly efficient catalyst. Overall, this study not only demonstrates the power of atomically precise metal clusters for achieving remarkable performances, but also promotes the exploration of new catalysts for existing catalysed processes. We believe that atomically precise metal clusters hold promise in both fundamental studies and industrial applications in homogeneous and heterogeneous catalysis.

Conflicts of interest

There are no conflicts to declare.

Data availability

CCDC 2416025 contains the supplementary crystallographic data for this paper.[53]

The data supporting this article have been included as a part of the SI. Supplementary information is available. See DOI: https://doi.org/10.1039/d5sc06255a.

Acknowledgements

We acknowledge financial support from the National Natural Science Foundation of China (22125202, 92461312, U24A20487, and 92361201) and SINOPEC Research Institute of Petroleum Processing Co., Ltd.

References

1 J. T. Grant, J. M. Venegas, W. P. McDermott and I. Hermans, *Chem. Rev.*, 2018, **118**, 2769–2815.
2 M. M. Montemore, M. A. van Spronsen, R. J. Madix and C. M. Friend, *Chem. Rev.*, 2018, **118**, 2816–2862.
3 D. Wang and D. Astruc, *Chem. Rev.*, 2015, **115**, 6621–6686.
4 X. Cai, H. Wang, Y. Tian, W. Ding and Y. Zhu, *ACS Catal.*, 2024, **14**, 11918–11930.
5 Z. W. Seh, J. Kibsgaard, C. F. Dickens, I. Chorkendorff, J. K. Nørskov and T. F. Jaramillo, *Science*, 2017, **355**, eaad4998.
6 J. Zhu, L. Hu, P. Zhao, L. Y. S. Lee and K.-Y. Wong, *Chem. Rev.*, 2020, **120**, 851–918.
7 M. Aresta, A. Dibenedetto and A. Angelini, *Chem. Rev.*, 2014, **114**, 1709–1742.
8 A. Wang, J. Li and T. Zhang, *Nat. Rev. Chem.*, 2018, **2**, 65–81.
9 Z. Li, S. Ji, Y. Liu, X. Cao, S. Tian, Y. Chen, Z. Niu and Y. Li, *Chem. Rev.*, 2020, **120**, 623–682.
10 L. Liu and A. Corma, *Chem. Rev.*, 2018, **118**, 4981–5079.
11 H. Seong, V. Efremov, G. Park, H. Kim, J. S. Yoo and D. Lee, *Angew. Chem., Int. Ed.*, 2021, **60**, 14563–14570.
12 R. Jin, G. Li, S. Sharma, Y. Li and X. Du, *Chem. Rev.*, 2021, **121**, 567–648.
13 S. Mitchell, R. Qin, N. Zheng and J. Pérez-Ramírez, *Nat. Nanotechnol.*, 2021, **16**, 129–139.
14 Y. Du, H. Sheng, D. Astruc and M. Zhu, *Chem. Rev.*, 2020, **120**, 526–622.
15 X. Liu, X. Cai and Y. Zhu, *Acc. Chem. Res.*, 2023, **56**, 1528–1538.
16 X. Cai, W. Hu, S. Xu, D. Yang, M. Chen, M. Shu, R. Si, W. Ding and Y. Zhu, *J. Am. Chem. Soc.*, 2020, **142**, 4141–4153.
17 T. Sun, B. Ge, S. Huang, X. Wang, Y. Tian, X. Cai, W. Ding and Y. Zhu, *Angew. Chem., Int. Ed.*, 2025, **64**, e202420274.
18 H. Bipp and H. Kieczka, *Ullmann's Encyclopedia of Industrial Chemistry*, Wiley-VCH, Weinheim, Germany, 2003.
19 C. J. Gerack and L. McElwee-White, *Molecules*, 2014, **19**, 7689–7713.
20 S. Ding and N. Jiao, *Angew. Chem., Int. Ed.*, 2012, **51**, 9226–9237.
21 M. W. Farlow and H. Adkins, *J. Am. Chem. Soc.*, 1935, **57**, 2222–2223.
22 P. G. Jessop, Y. Hsiao, T. Ikariya and R. Noyori, *J. Am. Chem. Soc.*, 1994, **116**, 8851–8852.
23 L. Zhang, Z. Han, X. Zhao, Z. Wang and K. Ding, *Angew. Chem., Int. Ed.*, 2015, **54**, 6186–6189.
24 G. Wang, M. Jiang, G. Ji, Z. Sun, C. Li, L. Yan and Y. Ding, *ACS Sustainable Chem. Eng.*, 2020, **8**, 5576–5583.
25 Y. Ma, C. Chen, Y. Jiang, X. Wei, Y. Liu, H. Liao, H. Wang, S. Dai, P. An and Z. Hou, *ACS Catal.*, 2023, **13**, 10295–10308.
26 Y. Shen, Q. Zheng, Z. N. Chen, D. Wen, J. H. Clark, X. Xu and T. Tu, *Angew. Chem., Int. Ed.*, 2021, **60**, 4125–4132.
27 D. Cheng, M. Wang, L. Tang, Z. Gao, X. Qin, Y. Gao, D. Xiao, W. Zhou and D. Ma, *Angew. Chem., Int. Ed.*, 2022, **61**, e202202654.
28 Q. Y. Bi, J. D. Lin, Y. M. Liu, S. H. Xie, H. Y. He and Y. Cao, *Chem. Commun.*, 2014, **50**, 9138–9140.
29 X. Cui, Y. Zhang, Y. Deng and F. Shi, *Chem. Commun.*, 2014, **50**, 13521–13524.
30 Y. Zhang, H. Wang, H. Yuan and F. Shi, *ACS Sustainable Chem. Eng.*, 2017, **5**, 5758–5765.
31 Q. Zou, J. Chen, Y. Wang, J. Gu, F. Liu and T. Zhao, *ACS Sustainable Chem. Eng.*, 2021, **9**, 16153–16162.
32 R. Li, Y. Zhao, H. Wang, J. Xiang, Y. Wu, B. Yu, B. Han and Z. Liu, *Chem. Sci.*, 2019, **10**, 9822–9828.
33 H. Liu, Q. Mei, Q. Xu, J. Song, H. Liu and B. Han, *Green Chem.*, 2017, **19**, 196–201.
34 Y. Wu, T. Wang, H. Wang, X. Wang, X. Dai and F. Shi, *Nat. Commun.*, 2019, **10**, 2599.
35 X. Dai, T. Li, B. Wang, C. Kreyenschulte, S. Bartling, S. Liu, D. He, H. Yuan, A. Brückner, F. Shi, J. Rabeah and X. Cui, *Angew. Chem., Int. Ed.*, 2023, **62**, e202217380.
36 C. Federsel, A. Boddien, R. Jackstell, R. Jennerjahn, P. J. Dyson, R. Scopelliti, G. Laurenczy and M. Beller, *Angew. Chem., Int. Ed.*, 2010, **49**, 9777–9780.
37 C. Ziebart, C. Federsel, P. Anbarasan, R. Jackstell, W. Baumann, A. Spannenberg and M. Beller, *J. Am. Chem. Soc.*, 2012, **134**, 20701–20704.
38 U. Jayarathne, N. Hazari and W. H. Bernskoetter, *ACS Catal.*, 2018, **8**, 1338–1345.
39 T. Mitsudome, T. Urayama, S. Fujita, Z. Maeno, T. Mizugaki, K. Jitsukawa and K. Kaneda, *ChemCatChem*, 2017, **9**, 3632–3636.
40 J. Mu, J. Liu, Z. Ran, M. Arif, M. Gao, C. Wang and S. Ji, *Ind. Eng. Chem. Res.*, 2020, **59**, 6543–6555.
41 J. Zhang, G. Li, J. Xie, Y. Hai, W. Wan, H. Sun, B. Wang, X. Wu, J. Cheng, C. He, W. Hu, Y. Zhang, Z. Li and C. Li, *J. Am. Chem. Soc.*, 2025, **147**, 3152–3160.
42 M. Walter, J. Akola, O. Lopez-Acevedo, P. D. Jadzinsky, G. Calero, C. J. Ackerson, R. L. Whetten, H. Grönbeck and H. A. Häkkinen, *Proc. Natl. Acad. Sci. U. S. A.*, 2008, **105**, 9157–9162.
43 C. M. Aikens, *Acc. Chem. Res.*, 2018, **51**, 3065–3073.
44 G. Li, C. Zeng and R. Jin, *J. Am. Chem. Soc.*, 2014, **136**, 3673–3679.
45 B. K. Teo, X. Shi and H. Zhang, *J. Am. Chem. Soc.*, 1992, **114**, 2743–2745.
46 C. M. Woodbridge, D. L. Pugmire, R. C. Johnson, N. M. Boag and M. A. Langell, *J. Phys. Chem. B*, 2000, **104**, 3085–3093.

47 Q. Yuan, T. Li, H. Lin, S. Huang, X. Huang, Y. Jing and Y. Zhu, *Adv. Funct. Mater.*, 2025, **35**, 2424623.
48 Z. Bacsik and N. Hedin, *Vib. Spectrosc.*, 2016, **87**, 215–221.
49 G. Li, J. Hou, X. Lei, D. Li, E. Yu, W. Hu, X. Cai, Xu. Liu, M. Chen and Y. Zhu, *Angew. Chem., Int. Ed.*, 2023, **62**, e202216735.
50 B. C. Smith, *Spectroscopy*, 2018, **33**, 14–20.
51 M. Yang, J. Zou, G. Wang and S. Li, *J. Phys. Chem. A*, 2017, **121**, 1351–1361.
52 G. Li, Z. Li, L. Gao, S. Chen, G. Wang and S. Li, *Phys. Chem. Chem. Phys.*, 2023, **25**, 23696–23707.
53 G. Li, G. Li, X. Liang, Y. Tian, J. Lu, X. Xu, X. Liu, J. Ma, S. Li and Y. Zhu, CCDC 2416025: Experimental Crystal Structure Determination, 2025, DOI: **10.5517/ccdc.csd.cc2m3294**.